Journal of Industrial and Engineering Chemistry 57 (2018) 284–289

Contents lists available at ScienceDirect

Journal of Industrial and Engineering Chemistry

journal homepage: www.elsevier.com/locate/jiec

High-performance Li-ion hybrid supercapacitors based on microporous pyropolymer nanoplates and orthorhombic Nb_2O_5 nanocomposites

Min Eui Lee[a,1], Se Youn Cho[a,1], Hyeon Ji Yoon[a], Young Soo Yun[b,*], Hyoung-Joon Jin[a,*]

[a] Department of Polymer Science and Engineering, Inha University, Incheon 22212, South Korea
[b] Department of Chemical Engineering, Kangwon National University, Samcheok 25913, South Korea

ARTICLE INFO

Article history:
Received 9 June 2017
Received in revised form 7 August 2017
Accepted 17 August 2017
Available online 24 August 2017

Keywords:
Hybrid supercapacitor
Pyropolymer
Niobium oxide
Nanocomposite
Electrode

ABSTRACT

In this study, high-performance Li-ion hybrid supercapacitors (LIHSs) were realized by the sophisticated design of nanostructured electrode pairs demonstrating both energy and kinetic balance. Microporous pyroprotein nanoplates (M-PNPs) were fabricated by a controlled pyrolysis process using potassium hydroxide, to achieve high electrochemical performance in the cathodic voltage region of 2.0–4.5 V *vs.* Li^+/Li. M-PNP/T-Nb_2O_5 nanocomposites obtained by introducing niobium oxide (T-Nb_2O_5) nanoparticles on the surface of M-PNP also showed outstanding Li-ion storage kinetics in the anodic voltage range of 1.0–2.0 *vs.* Li^+/Li. The LIHSs based on M-PNP and M-PNP/T-Nb_2O_5 nanocomposite samples used as the cathode and anode pair, respectively, exhibited a high specific energy of ~47.5 W h kg^{-1} at ~280.0 W kg^{-1} and a high specific power of ~10,000 W kg^{-1} at ~22.3 W h kg^{-1} with excellent cycling stability over 30,000 cycles.

Introduction

Hybrid supercapacitors exhibit higher energy characteristics and faster kinetic performances than those of conventional supercapacitors or rechargeable batteries, because they use a battery-like faradic electrode and capacitive non-faradic electrode pair in asymmetric configurations [1–3]. The redox reactions of typical faradic electrodes occur at all equivalent redox sites of the bulk host structures through the solid-state diffusion of charges; the electrodes show high charge storage capacities but poor rate performances [4]. In contrast, conventional non-faradic electrodes exhibit rapid charge-storage characteristics by the physical adsorption and desorption of solvated charges in the electrode–electrolyte interfacial areas; however, their energy capacities are limited [5,6]. These energy and kinetic imbalances between the two different types of electrodes can impair hybrid supercapacitors. Therefore, considerable efforts have been devoted to design an optimal electrode assembly with better-performing active materials [2,7–14].

Niobium pentoxide (Nb_2O_5) is a promising host material for pseudocapacitive Li ion storage; it exhibits exceptionally high power and good energy performance [15,16]. Moreover, the crystal structure of Nb_2O_5 shows no apparent phase transition or volume change upon Li-ion insertion/extraction, enabling stable cyclability [15,16]. The theoretical capacity of Nb_2O_5 for Li-ion storage is ~730 C g^{-1}, most of which is concentrated in the voltage range of 1–2 V *vs.* Li^+/Li, and can potentially serve as an anode for Li-ion hybrid supercapacitors (LIHSs) [17]. However, the fast Li-ion storage performance of Nb_2O_5 is hindered by its poor electrical conductivity (~3.4×10^{-6} S cm^{-1}); therefore, many studies have focused on enhancing the rate capabilities of Nb_2O_5-based electrode materials [18,19]. Among various strategies for improving the power capability, use of nanocomposites comprising few-nanometer-scale Nb_2O_5 and a conductive carbon nanomatrix is the best, because they show synergistic charge-storage behaviors as well as nanometer-scale effects such as nanoionics and nanoelectronics [20–23]. Furthermore, the nanocomposites may experience less fatigue in repetitive cycling tests, because they are characterized by large surface-to-volume ratios and show pseudocapacitive charge-storage mechanisms. However, reports on Nb_2O_5-based nanocomposite materials as electrodes for energy storage have been rare.

* Corresponding authors.
E-mail addresses: ysyun@kangwon.ac.kr (Y.S. Yun), hjjin@inha.ac.kr (H.-J. Jin).
[1] These authors contributed equally to this work.

http://dx.doi.org/10.1016/j.jiec.2017.08.034
1226-086X/

Pyroproteins are carbon-based materials fabricated from protein precursors by a simple heating process; they possess a number of redox-active heteroatoms and amorphous carbon microstructures [24]. Several studies have demonstrated that functionalized carbonaceous materials can store charges over wide operating voltage windows, permitting exceptionally high power and high energy performance with a long-term cycle life [6,10,14,25,26]. Lee et al. reported oxygen-functionalized carbon nanotubes as cathode materials for Li-ion storage, with a high specific capacity of ~200 mA h g^{-1} and lifetime of thousands of cycles [27]. Kim et al. reported the relationship between the O-containing functional groups and specific capacity of graphene-based electrode materials for Li-ion storage [28]. In addition, synergistic charge-storage behaviors of O and N were revealed in the cathodic voltage region [29]. These results suggest that combinations of nanostructured pyroproteins and Nb_2O_5 nanoparticles could be appropriate nanocomposite materials for use as anodes in LIHSs, while nanostructured pyroproteins could serve as cathode materials for Li-ion storage.

In this study, microporous pyroprotein nanoplates (M-PNPs) were fabricated from regenerated silk protein by simply heating it with potassium hydroxide, and orthorhombic Nb_2O_5 (T-Nb_2O_5) nanoparticles were introduced on the M-PNP surface. The M-PNPs and M-PNP/T-Nb_2O_5 nanocomposites showed high capacitances of 276 and 213 F g^{-1} in the voltage ranges of 1.0–2.0 and 2.0–4.5 V, respectively, with remarkably high rate capabilities. In addition, LIHSs based on M-PNP and M-PNP/T-Nb_2O_5 nanocomposite samples as cathode and anode, respectively, produced a maximum specific energy and power of 47.5 W h kg^{-1} and 10,000 W kg^{-1}, respectively, with stable cycling performances over 30,000 cycles.

Experimental

Preparation of the M-PNP/T-Nb_2O_5 nanocomposite

Bombyx mori silk fibroin solutions were prepared following a procedure reported elsewhere [26]. The sericin protein was removed from the cocoons of *B. mori* silkworms *via* treatment in a boiling aqueous solution of Na_2CO_3 (OCI Company, 99%, 0.02 M) for 30 min. The extracted silk fibroin was regenerated in a strong alkali solution of 9.3 M LiBr (Sigma–Aldrich, ≥99%) at room temperature and dialyzed in distilled water using Slide-A-Lyzer dialysis cassettes (Pierce, MWCO 3500) for 48 h. Then, 4 g of KOH was dissolved in 100 g of the 8 wt% regenerated silk fibroin solution and the resulting solution was dried in a convection oven at 120 °C. The silk fibroin/KOH mixture was then heated in a tubular furnace to 800 °C at a heating rate of 10 °C min^{-1} under an Ar flow at 200 mL min^{-1} and held at the final temperature for 2 h. The resulting product, was thoroughly rinsed with ethanol and distilled water and dried in a vacuum oven at 30 °C to obtain the M-PNP sample.

Then, 0.15 g M-PNPs was immersed in 50 mL of distilled water containing 0.375 g of the $NbCl_5$ precursor and ultrasonicated for 30 min. After drying in a convection oven at 80 °C, the mixture was heated in a tubular furnace to 800 °C at a heating rate of 10 °C min^{-1} under a flow of Ar at 200 mL min^{-1} and held at the final temperature for 2 h.

Characterization

The morphologies of the samples were examined by field-emission scanning electron microscopy (FE-SEM, S-4300SE, Hitachi, Japan) and field-emission transmission electron microscopy (FE-TEM, JEM2100F, JEOL, Japan). T-Nb_2O_5 contents in the nanocomposites were confirmed by thermogravimetric analysis (TGA, Q50, TA instruments, UK) in the temperature range of 20–800 °C at a heating rate of 10 °C min^{-1} in air. Raman spectra were recorded using a continuous-wave linearly polarized laser (514.5 nm, 2.41 eV, 16 mW). The laser beam was focused using a 100× objective lens, to obtain a spot of ~1 μm diameter. The acquisition time and number of cycles used to collect each spectrum were 10 s and 3, respectively. X-ray diffraction (XRD, Rigaku DMAX 2500) was performed using Cu-K_α radiation (λ = 0.154 nm) at 40 kV and 100 mA. The chemical composition of the samples was examined by X-ray photoelectron spectroscopy (XPS, PHI 5700 ESCA, USA) using monochromatic Al-K_α radiation ($h\nu$ = 1486.6 eV). The pore structure of the samples was analyzed using N_2 adsorption and desorption isotherms obtained by a surface area and porosimetry analyzer (ASAP 2020, Micromeritics, USA) at −196 °C.

Electrochemical characterization

The electrochemical properties of the M-PNPs, M-PNP/T-Nb_2O_5 nanocomposites, and full-cell energy storage devices based on them were characterized using a WonATech automatic battery cycler and CR2032-type coin cells. To fabricate half-cells, the coin cells were assembled in an Ar-filled glove box using M-PNP or M-PNP/T-Nb_2O_5 nanocomposite sample as the working electrode and metallic Li foils as both the reference and counter electrodes. 1 M $LiClO_4$ (Aldrich, 99.99%) was dissolved in propylene carbonate (PC, Sigma–Aldrich, purity: anhydrous, 99.7%, USA) and used as the electrolyte for Li-ion storage. A glass microfiber filter (GF/F, Whatman) was used as a separator. The working electrodes were prepared by mixing the active material (80 wt%) with conductive carbon (10 wt%; Alfa Aesar Co., purity: >99%, England) and polyvinylidene fluoride (10 wt.%; Sigma–Aldrich, USA) in *N*-methyl-2-pyrrolidone (OCI Co., 99.9%, USA). The resulting slurry was uniformly applied to an Al foil (Wellcos Co., Korea). The electrodes were dried at 120 °C for 2 h and roll-pressed. The loading of the active material was ~1 mg cm^{-2}, and the total electrode weight was ~1–2 mg. To create full cells, the coin cells were assembled in a glove box filled with Ar. The same electrolyte and separator were used, and the total electrode weight of both the anode and cathode was 4–5 mg.

For testing the half-cells, the anode and cathode were galvanostatically cycled between 1.0 and 2.0 V *vs.* Li/Li^+ and between 2.0 V and 4.5 V *vs.* Li/Li^+, respectively, at various specific currents. In addition, the full cells were galvanostatically cycled between 0 and 3.5 V. To assemble the full cells, the anode and cathode were pre-cycled with Li metal for several cycles, and the onset potential of both electrodes was controlled at 2.0 V *vs.* Li/Li^+.

Results and discussion

The morphologies of the M-PNPs were characterized by FE-TEM and AFM images (Fig. 1). M-PNPs have a high aspect ratio above ~100 with lateral sizes of several micrometers and tens of nanometer thicknesses (Fig. 1(a, b, and d)). In addition, the high-resolution FE-TEM image reveals that M-PNPs have an amorphous carbon structure with no long-range carbon ordering (Fig. 1(c)). Remarkably, despite the poor development of aromatic carbon domains, the M-PNP particles show remarkable electrical properties including conductivities reaching ~36 S cm^{-1} at room temperature, as characterized by the four-probe method (Fig. 1(e and f)). T-Nb_2O_5 nanoparticles were introduced on the surfaces of the M-PNPs by soaking the nanoplates in an aqueous solution containing $NbCl_5$ precursor and then simply heating the mixture to 800 °C under N_2 atmosphere (Fig. 2(a)). The resulting loading content of T-Nb_2O_5 nanoparticles was confirmed by TGA in air, which is ~60 wt% T-Nb_2O_5 in the nanocomposite (Fig. S1). However, the introduced T-Nb_2O_5 nanoparticles are not observed

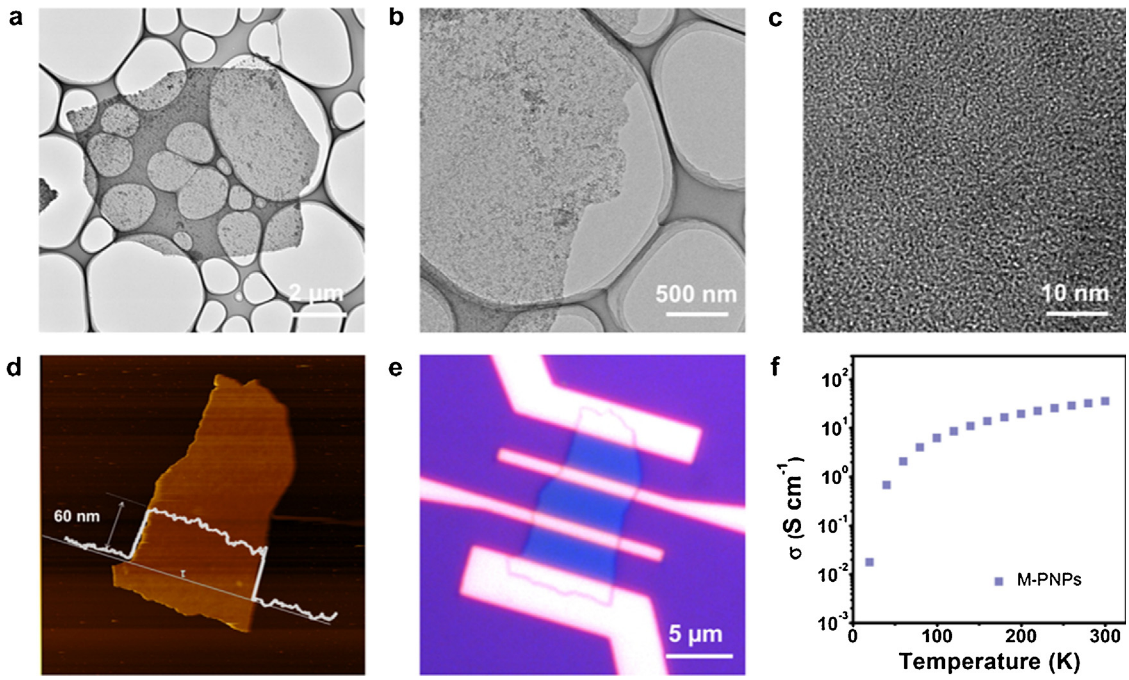

Fig. 1. (a and b) FE-TEM images of M-PNPs at different magnifications. (c) High-resolution FE-TEM image of M-PNPs. (d) AFM image of M-PNPs with a line profile showing the thickness. (e) Optical image of a M-PNP mound in the four-electrode configuration and (f) temperature-dependent electrical properties measured from 20 to 300 K.

in the FE-SEM image of the M-PNP/T-Nb_2O_5 nanocomposite (Fig. 2(b)), indicating that the T-Nb_2O_5 nanoparticles are too small to be detected and are well-dispersed on the surfaces of the M-PNPs without aggregation. Therefore, the presence of the T-Nb_2O_5 nanoparticles was confirmed by FE-TEM images (Fig. 2(c and d)). T-Nb_2O_5 nanoparticles, measuring ~2–5 nm, were homogeneously distributed on the M-PNPs (Fig. 2(c and d)). The T-Nb_2O_5 nanoparticles are formed from hydrated Nb^+ ions adsorbed on the surfaces of the M-PNPs through the decomposition of water molecules; the combination of Nb^+ and the resulting O_2 during the thermal treatment process creates T-Nb_2O_5, as depicted schematically in Fig. 2(a).

The microstructure of the M-PNPs and M-PNP/T-Nb_2O_5 nanocomposite was examined by Raman spectra and XRD as shown in Fig. 3(a and b). It is noteworthy that the Raman spectra of the M-PNPs and M-PNP/T-Nb_2O_5 nanocomposite have similar

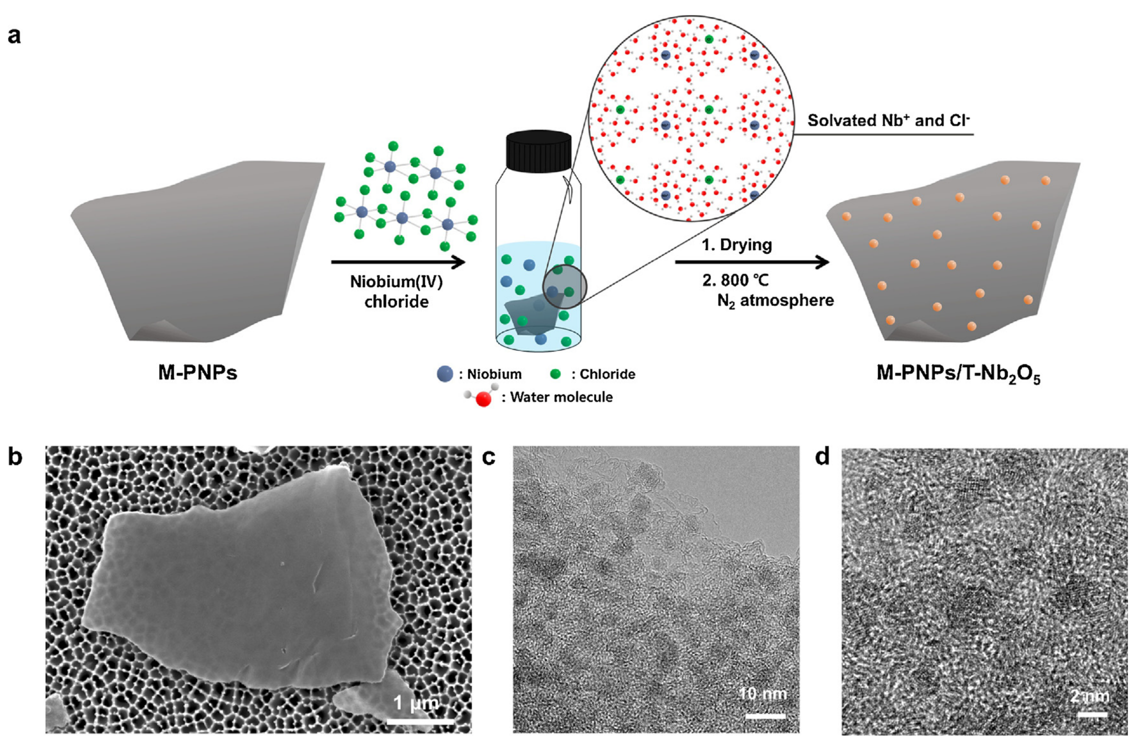

Fig. 2. (a) Schematic of the preparation of M-PNP/T-Nb_2O_5 nanocomposite. (b) FE-SEM image and (c and d) high-resolution FE-TEM images of the M-PNP/T-Nb_2O_5 nanocomposite at different magnifications.

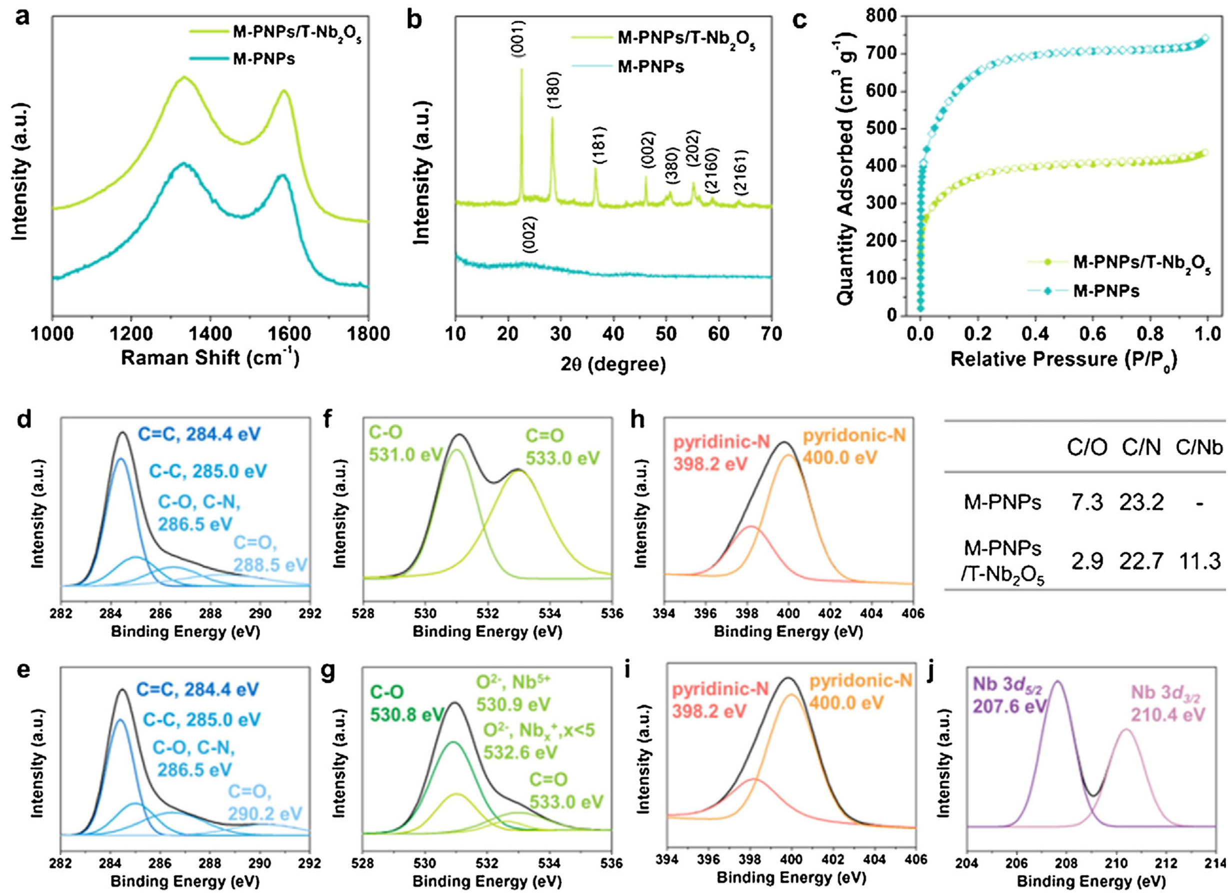

	C/O	C/N	C/Nb
M-PNPs	7.3	23.2	-
M-PNPs /T-Nb_2O_5	2.9	22.7	11.3

Fig. 3. (a) Raman spectra, (b) XRD patterns, and (c) N_2 adsorption and desorption isotherms of the M-PNPs and M-PNP/T-Nb_2O_5 nanocomposite. XPS: (d) C, (f) O, and (h) N 1*s* spectra of M-PNPs and (e) C, (g) O, (i) N 1*s*, and (j) Nb 3*d* spectra of the M-PNP/T-Nb_2O_5 nanocomposite.

shapes with clear characteristic *D* and *G* bands attributed to carbon at ~1335 and ~1580 cm^{-1}, respectively (Fig. 3(a)); these correspond to the disordered A_{1g} breathing mode of the six-membered aromatic ring close to the basal edge and the E_{2g} vibration mode of the sp^2-hybridized C atoms related to the hexagonal carbon structure, respectively [30]. Therefore, from the intensity ratio of the *D* to *G* peaks (I_D/I_G), the approximate size of the poly-hexagonal carbon structures can be calculated. The I_D/I_G values of the M-PNPs and M-PNP/T-Nb_2O_5 nanocomposite are similar at ~1.12, indicating that they both contain carbon crystal domains, several nanometers in size. In contrast to the Raman spectra, which exhibit similar peak positions and intensities, the XRD patterns of the M-PNPs and M-PNP/T-Nb_2O_5 are different because of the presence of T-Nb_2O_5 nanoparticles in the nanocomposite (Fig. 3(b)). Several sharp peaks centered at 22.5, 28.4, 36.6, 46.2, and 55.2°, originating from the (001), (180), (181), (002), and (202) planes of T-Nb_2O_5, respectively, are found in the pattern of the nanocomposite, whereas the pattern of the M-PNPs shows a single broad peak from the amorphous carbon structure. These results confirm that the T-Nb_2O_5 nanoparticles are deposited on the M-PNPs without affecting the M-PNP carbon structure.

The pore structure of the M-PNPs and M-PNP/T-Nb_2O_5 nanocomposite was investigated by N_2 adsorption and desorption isotherm curves (Fig. 3(c)). The isotherm of the M-PNPs reveals a high adsorption capacity in the low relative pressure region of <0.02, indicating very high monolayer adsorption of N_2 molecules on the surfaces of the M-PNPs. In addition, the isotherm curve shows a slight increase in the quantity of adsorbed N_2 in the relative pressure region of 0.2–1.0 without any hysteresis between the adsorption and desorption curves, indicating an IUPAC type-I microporous structure. Because of the highly developed nanometer-scale pores, the M-PNPs present a high specific surface area of 2347.7 $m^2\,g^{-1}$. After the deposition of T-Nb_2O_5 nanoparticles on the M-PNPs, the isotherm shows a similar shape, corresponding to the IUPAC type-I microporous structure, however, the specific surface area of the nanocomposite is significantly reduced to 1330.1 $m^2\,g^{-1}$. The decrease in the specific surface area is more likely caused by the introduction of T-Nb_2O_5, rather than by the deterioration of the pore structure.

The surface chemical structure of the M-PNPs and M-PNP/T-Nb_2O_5 nanocomposite was characterized by XPS, as shown in Fig. 3(d–j). In the C 1*s* spectra of M-PNPs, several carbon bonding structures such as C=C, C—C, C—O, C—N, and C=O are detected (Fig. 3(d)) [31]. After the deposition of the T-Nb_2O_5 nanoparticles on the surfaces of the M-PNPs, the peak position of the C=O bond centered at 288.5 eV is shifted to a higher binding energy of ~290.2 eV, suggesting the interaction between the M-PNPs and T-Nb_2O_5 nanoparticles (Fig. 3(e)). The O 1*s* spectrum of the M-PNPs shows C—O and C=O bonding peaks centered at ~531.0 and ~533.0 eV, respectively (Fig. 3(f)). In particular, the O 1*s* spectra of the nanocomposite show two distinct additional chemical structures of Nb and O, originating mainly from the fully oxidized O^{2-} state at 530.9 eV and the minor defective NbO_x state at 532.6 eV (Fig. 3(g)) [32]. The nanometer-scale T-Nb_2O_5 inevitably has many free edges and vacancy defects, and presents numerous defective sites. Furthermore, both samples show signals corresponding to the N-groups of the pyridinic-N and pyridonic-N structures centered at 398.2 and 400.0 eV, respectively, as shown

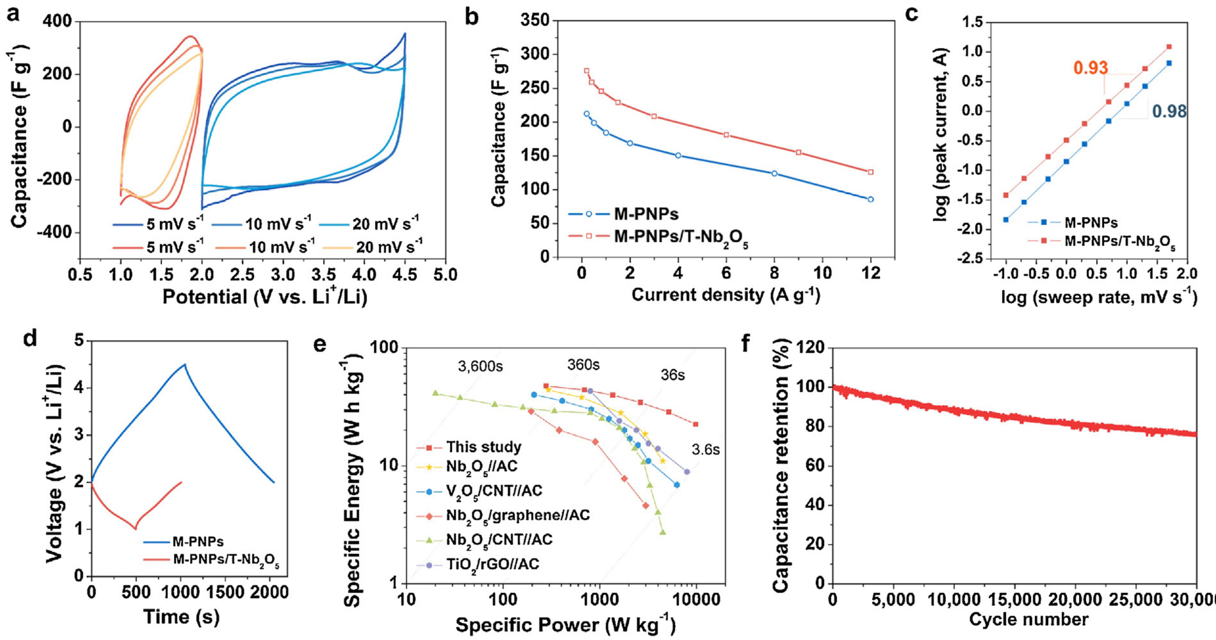

Fig. 4. Electrochemical performances of M-PNPs and M-PNP/T-Nb_2O_5 nanocomposite, and full cell devices (LIHSs) characterized in an electrolyte of 1 M $LiClO_4$ dissolved in PC over different voltage windows of 2.0–4.5 and 1.0–2.0 V *vs.* Li^+/Li for the M-PNPs and M-PNP/T-Nb_2O_5 nanocomposite, respectively, and 0–3.5 V for the LIHSs. (a) CVs at sweep rates from 5 to 20 mV s^{-1}, (b) rate capabilities at current densities ranging from 0.2 to 12 A g^{-1}, (c) specific peak currents at different sweep rates, and (d) galvanostatic charge/discharge profiles of the M-PNPs and M-PNP/T-Nb_2O_5 nanocomposite at a current rate of 0.5 A g^{-1}. (e) The Ragone plot of several energy storage devices including the LIHSs. (f) Cycling performance of the LIHSs over 30,000 cycles.

in the XPS N 1*s* spectra (Fig. 3(h and i)) [31]. The N and O groups on the M-PNPs may act as redox hosts for pseudocapacitive Li-ion storage, which may contribute to the overall charge storage capacity along with the T-Nb_2O_5 nanoparticles in the nanocomposite [29]. The Nb 3*d* spectrum of the nanocomposite shows clear Nb $3d_{5/2}$ and Nb $3d_{3/2}$ peaks at 207.6 and 210.4 eV, respectively, supporting the presence of T-Nb_2O_5 nanoparticles (Fig. 3(j)) [23].

The electrochemical performance of the M-PNPs and M-PNP/T-Nb_2O_5 nanocomposite was tested in the voltage ranges of 1.0–2.0 and 2.0–4.5 *vs.* Li^+/Li, respectively, in 1 M $LiClO_4$ dissolved in a solution of PC used as the electrolyte (Fig. 4). Cyclovoltammograms (CVs) of the M-PNPs show nearly rectangular shapes, indicating capacitive charge-storage behavior, whereas those of the M-PNP/T-Nb_2O_5 nanocomposites exhibit atypical shapes with protrusions because of the pseudocapacitive mechanism (Fig. 4(a)). The CVs of both samples maintain their shapes at different sweep rates ranging from 5 to 20 mV s^{-1}. In case of the M-PNP/T-Nb_2O_5 nanocomposite, the hybrid charge-storage mechanism based on dual capacitive charge storage and pseudocapacitive reactions facilitates a high specific capacitance of 276 F g^{-1} at the current density of 0.2 A g^{-1}, which is gradually decreased with increasing current densities (259, 246, 229, 209, 181, 155, and 126 F g^{-1} at 0.2, 0.4, 0.8, 1.5, 3, 6, 9, and 12 A g^{-1}, respectively). These capacitance values are higher than those of M-PNPs (213, 199, 184, 169, 150, 124, and 86 F g^{-1} at 0.2, 0.5, 1, 2, 4, 8, and 12 A g^{-1}, respectively) at all tested current densities (Fig. 4(b)). Whereas the specific capacitances of the M-PNPs and M-PNP/T-Nb_2O_5 nanocomposites differ, their rate capabilities are nearly same (Fig. 4(b)). The charge storage kinetics of both samples was investigated from the CV curves obtained at different sweep rates (Fig. 4(c)). The peak currents increase with increasing sweep rates, which can be mathematically expressed as, $i = av^b$, where *a* and *b* are adjustable parameters [15]. The charge storage mechanism can be assessed from the *b*-value [23]. If the sample shows a *b*-value close to 0.5, the charge storage mechanism is diffusion-controlled. In contrast, a *b*-value close to 1 indicates surface control. The M-PNPs and M-PNP/T-Nb_2O_5 nanocomposites show *b*-values of 0.98 and 0.93, respectively, indicating that their charge storage mechanisms are mainly surface-controlled [33]. The galvanostatic charge/discharge profiles of the M-PNPs and M-PNP/T-Nb_2O_5 nanocomposite characterized in the different voltage ranges of 2.0–4.5 and 1.0–2.0 V, respectively, are depicted in Fig. 4(d). Both profiles are almost linear, which is consistent with the CV results. Because the operating voltage of M-PNPs is 2.5 folds larger than that of the M-PNP/T-Nb_2O_5 nanocomposite, the discharge/charge time of M-PNPs is approximately twice as long. Therefore, asymmetric LIHSs based on the M-PNPs and M-PNP/T-Nb_2O_5 nanocomposite samples as cathode and anode, respectively, were assembled with double anode contents to adjust the energy balance between the two electrodes (Fig. S2). In addition, through charge injection, the initial voltage of both electrodes was set to 2.0 V *vs.* Li^+/Li and the LIHSs were operated in the voltage window of 0–3.5 V (Fig. S2) [32]. The electrochemical performances of the LIHSs are confirmed in the Ragone plot, which compares different energy storage devices (Fig. 4(e)). For the LIHSs, a maximum specific energy of 47.5 W h kg^{-1} at the specific power of ~280.0 W kg^{-1} is achieved. The LIHSs show a maximum power of ~10,000 W kg^{-1} at 22.3 W h kg^{-1}, indicating remarkable energy and power characteristics. These values surpass those of previously reported energy storage devices such as Nb_2O_5/AC [34], V_2O_5/carbon nanotube (CNT)/AC [35], Nb_2O_5/graphene/AC [36], Nb_2O_5/CNT/AC [37], and TiO_2/rGO/AC [2]. Furthermore, the LIHSs demonstrate outstanding cycling performance over 30,000 cycles with 75% capacitance retention relative to the initial capacitance.

Conclusion

M-PNPs with amorphous carbon structures were prepared from regenerated silk protein *via* pyrolysis with potassium hydroxide at 800 °C. The M-PNPs have high aspect ratios of >100, electrical conductivities of ~36 S cm^{-1}, specific surface areas of ~2347.7 $m^2 g^{-1}$, and numerous O and N heteroatoms (C/O and C/N ratios of 7.3 and 23.2, respectively). Few-nanometer-sized T-Nb_2O_5 nanoparticles were introduced on the surfaces of the M-PNPs; the composite showed a high specific capacitance of 276 $F g^{-1}$ in the voltage range of 1.0–2.0 V *vs.* Li^+/Li. In contrast, the M-PNPs exhibited a high specific capacitance of 213 $F g^{-1}$ in the voltage window of 2.0–4.5 V. The charge storage kinetics of both M-PNPs and the M-PNP/T-Nb_2O_5 nanocomposite was surface-controlled, while both systems exhibited high rate capabilities. LIHSs based on M-PNPs and M-PNP/T-Nb_2O_5 nanocomposite as cathode and anode materials, respectively, were assembled after charge injection. They operated in the wide voltage window of 0–3.5 V, with high specific energy and power characteristics of ~47.5 W h kg^{-1} and ~10,000 W kg^{-1}, respectively, and displayed outstanding cycling performance over 30,000 cycles.

Acknowledgment

This research was supported by the Basic Science Research Program through the National Research Foundation of Korea (NRF) funded by the Ministry of Education (NRF-2016R1A2B4009601). This work was also supported by Industrial Strategic Technology Development Program, (Project No. 10050477, Development of separator with low thermal shrinkage and electrolyte with high ionic conductivity for Na-ion batteries) funded by the Ministry of Trade, Industry & Energy (MI, Korea). Additional support was provided by the Korea Institute of Energy Technology Evaluation and Planning (KETEP) and the Ministry of Trade, Industry & Energy (MOTIE) of the Republic of Korea (No. 20145020300980).

Appendix A. Supplementary data

Supplementary data associated with this article can be found, in the online version, at http://dx.doi.org/10.1016/j.jiec.2017.08.034.

References

[1] F. Zhang, T. Zhang, X. Yang, L. Zhang, K. Leng, Y. Huang, Y. Chen, Energy Environ. Sci. 6 (2013) 1623.
[2] H. Kim, M.-Y. Cho, M.-H. Kim, K.-Y. Park, H. Gwon, Y. Lee, K.C. Roh, K. Kang, Adv. Energy Mater. 3 (2013) 1500.
[3] D.P. Dubal, O. Ayyad, V. Ruiz, P. Gómez-Romero, Chem. Soc. Rev. 44 (2015) 1777.
[4] M. Noel, V. Suryanarayanan, J. Power Sources 111 (2002) 193.
[5] P. Simon, Y. Gogotsi, B. Dunn, Science 343 (2014) 1210.
[6] Y.S. Yun, S.Y. Cho, J. Shim, B.H. Kim, S.-J. Chang, S.J. Baek, Y.S. Huh, Y. Tak, Y.W. Park, S. Park, H.-J. Jin, Adv. Mater. 25 (2013) 1993.
[7] H. Wang, Y. Zhang, H. Ang, Y. Zhang, H.T. Tan, Y. Zhang, Y. Guo, J.B. Franklin, X.L. Wu, M. Srinivasan, H.J. Fan, Q. Yan, Adv. Funct. Mater. 26 (2016) 3082.
[8] J. Luo, W. Zhang, H. Yuan, C. Jin, L. Zhang, H. Huang, C. Liang, Y. Xia, J. Zhang, Y. Gan, X. Tao, ACS Nano 11 (2017) 2459.
[9] L. Shen, H. Lv, S. Chen, P. Kopold, P.A. van Aken, X. Wu, J. Maier, Y. Yu, Adv. Mater. (2017) 1700142, doi:http://dx.doi.org/10.1002/adma.201700142.
[10] N.R. Kim, S.Y. Cho, H.J. Yoon, H.-J. Jin, Y.S. Yun, Electrochim. Acta 222 (2016) 1887.
[11] A. Banerjee, K.K. Upadhyay, D. Puthusseri, V. Aravindan, S. Madhavi, S. Ogale, Nanoscale 6 (2014) 4387.
[12] E. Lim, H. Kim, C. Jo, J. Chun, K. Ku, S. Kim, H.I. Lee, I.-S. Nam, S. Yoon, K. Kang, J. Lee, ACS Nano 8 (2014) 8968.
[13] P. Sennu, V. Aravindan, Y.-S. Lee, Chem. Eng. J. 324 (2017) 26.
[14] M.Y. Song, N.R. Kim, S.Y. Cho, H.-J. Jin, Y.S. Yun, ACS Sustain. Chem. Eng. 5 (2017) 616.
[15] V. Augustyn, J. Come, M.A. Lowe, J.W. Kim, P.-L. Taberna, S.H. Tolbert, H.D. Abruña, P. Simon, B. Dunn, Nat. Mater. 12 (2013) 518.
[16] R. Kodama, Y. Terada, I. Nakai, S. Komaba, N. Kumagai, J. Electrochem. Soc. 153 (2006) A583.
[17] K. Brezesinski, J. Wang, J. Haetge, C. Reitz, S.O. Steinmueller, S.H. Tolbert, B.M. Smarsly, B. Dunn, T. Brezesinski, J. Am. Chem. Soc. 132 (2010) 6982.
[18] R.J. Cava, B. Batlogg, J.J. Krejewski, H.F. Poulsen, P.W.F. Gammel. Peck Jr., L.W. Rupp Jr., Phys. Rev. B 44 (1991) 6973.
[19] A.L. Viet, M.V. Reddy, B.V.R. Chowdari, S. Ramakrishna, J. Phys. Chem. C 114 (2010) 664.
[20] E. Lim, C. Jo, H. Kim, M.-H. Kim, Y. Mun, J. Chun, Y. Ye, J. Hwang, K.-S. Ha, K.C. Roh, K. Kang, S. Yoon, J. Lee, ACS Nano 9 (2015) 7497.
[21] L. Kong, C. Zhang, J. Wang, W. Qiao, L. Ling, D. Long, ACS Nano 9 (2015) 11200.
[22] L. Kong, C. Zhang, S. Zhang, J. Wang, R. Cai, C. Lv, W. Qiao, L. Ling, D. Long, J. Mater. Chem. A 2 (2014) 17962.
[23] M.Y. Song, N.R. Kim, H.J. Yoon, S.Y. Cho, H.-J. Jin, Y.S. Yun, ACS Appl. Mater. Interfaces 9 (2017) 2267.
[24] S.Y. Cho, Y.S. Yun, S. Lee, D. Jang, K.-Y. Park, J.K. Kim, B.H. Kim, K. Kang, D.L. Kaplan, H.-J. Jin, Nat. Commun. 6 (2015) 8145.
[25] Y.S. Yun, S.Y. Cho, H. Kim, H.-J. Jin, K. Kang, ChemElectroChem 2 (2015) 359.
[26] Y.S. Yun, K.-Y. Park, B. Lee, S.Y. Cho, Y.-U. Park, S.J. Hong, B.H. Kim, H. Gwon, H. Kim, S. Lee, Y.W. Park, H.-J. Jin, K. Kang, Adv. Mater. 27 (2015) 6914.
[27] S.W. Lee, N. Yabuuchi, B.M. Gallant, S. Chen, B.-S. Kim, P.T. Hammond, Y. Shao-Horn, Nat. Nanotechnol. 5 (2010) 531.
[28] H. Kim, H.-D. Lim, S.-W. Kim, J. Hong, D.-H. Seo, D. Kim, S. Jeon, S. Park, K. Kang, Sci. Rep. 3 (2013) 1506.
[29] Y.S. Yun, D.-H. Kim, S.J. Hong, M.H. Park, Y.W. Park, B.H. Kim, H.-J. Jin, K. Kang, Nanoscale 7 (2015) 15051.
[30] Y.S. Yun, G. Yoon, K. Kang, H.-J. Jin, Carbon 80 (2014) 246.
[31] S.Y. Cho, H.J. Yoon, N.R. Kim, Y.S. Yun, H.-J. Jin, J. Power Sources 329 (2016) 536.
[32] Z. Weng, F. Li, D.-W. Wang, L. Wen, H.-M. Cheng, Angew. Chem. Int. Ed. 52 (2013) 3722.
[33] L. Kong, C. Zhang, S. Zhang, J. Wang, R. Cai, C. Lv, W. Qiao, L. Ling, D. Long, J. Mater. Chem. A 2 (2014) 17962.
[34] J. Come, V. Augustyn, J.W. Kim, P. Rozier, P.-L. Taberna, P. Gogotsi, J.W. Long, B. Dunn, P. Simon, J. Electrochem. Soc. 161 (2014) A718.
[35] Z. Chen, V. Augustyn, J. Wen, Y. Zhang, M. Shen, B. Dunn, Y. Lu, Adv. Mater. 23 (2011) 791.
[36] L.P. Wang, L. Yu, R. Satish, J. Zhu, Q. Yan, M. Srinivasan, Z. Xu, RSC Adv. 4 (2014) 37389.
[37] X. Wang, G. Li, Z. Chen, V. Augustyn, X. Ma, G. Wang, B. Dunn, Y. Lu, Adv. Energy Mater. 1 (2011) 1089.